Eur. J. Mineral., 36, 813–830, 2024
https://doi.org/10.5194/ejm-36-813-2024

European Journal of Mineralogy
Open Access

Carbon-containing pyrite spherules: mineral biosignatures in black smokers?

Chloé Truong[1,a], **Sylvain Bernard**[1], **François Baudin**[2], **Aurore Gorlas**[3], **and François Guyot**[1,4]

[1]Institut de Minéralogie, de Physique des Matériaux et de Cosmochimie (IMPMC), Sorbonne Université, Museum National d'Histoire Naturelle, CNRS, Paris, France
[2]Institut des Sciences de la Terre de Paris (ISTeP), Sorbonne Université, CNRS, Paris, France
[3]Institute for Integrative Biology of the Cell (I2BC), Université Paris-Saclay, CEA, CNRS, Gif-sur-Yvette, France
[4]Institut Universitaire de France (IUF), Paris, France
[a]present address: Institut de Microbiologie de la Méditerranée (IMM), CNRS, Aix-Marseille Université (AMU), Marseille, France

Correspondence: Chloé Truong (ctruong@imm.cnrs.fr) and François Guyot (francois.guyot@mnhn.fr)

Received: 16 January 2024 – Revised: 25 June 2024 – Accepted: 17 July 2024 – Published: 18 September 2024

Abstract. Sulfide- and sulfate-rich hydrothermal vents are involved in Earth's major geochemical cycles. An outstanding scientific question consists of finding out whether certain minerals found in hydrothermal chimneys are influenced more or less directly by microorganisms living at high temperatures (thermophiles or hyperthermophiles) in these environments.

Here we report the morphological, textural and chemical characterization of pyrite crystals collected across a section of a chimney from the Trans-Atlantic Geotraverse hydrothermal site, sampled from the inner, hotter portion to the external, cooler portion, providing a promising approach to the search for hyperthermophilic biosignatures.

The internal and middle portions of the chimney mainly harbour cube-shaped pyrite containing low quantities of hydrocarbons and thermally matured organic compounds. In contrast, the samples from the external portion contain pyrite spherules composed of a mosaic of slightly disoriented domains that include large amounts of organic material chemically consistent with thermally matured biogenic organic compounds. These characteristics make them comparable but not identical to pyrite spherules produced in the laboratory in the presence of hyperthermophilic archaea of the order Thermococcales. Differences include larger crystalline domains and more thermally matured organic compounds. Such features could be consistent with the thermal transformation of pyrite spherules produced by (or at least in the presence of) living cells. However, it remains impossible to completely rule out an abiotic origin without further isotopic investigation and experimental studies on the abiotic production of pyrite spherules in the presence of organic compounds and under hydrothermal conditions.

1 Introduction

Sulfide-bearing hydrothermal vents and their associated ecosystems were discovered in 1977 (Corliss et al., 1979). The discovery of black smokers has given birth to new hypotheses (and controversies) about the emergence of life and its earliest evolution. In fact, the redox activity and chemical reactivity of minerals abundant in black smoker chimneys such as pyrite (FeS_2), chalcopyrite ($CuFeS_2$) and sphalerite (ZnS) may have promoted fundamental prebiotic processes (Huber and Wächtershäuser, 1997; Russell et al., 1994; Wächtershäuser, 1990). Furthermore, black smokers play a unique role in exchanging heat and chemical species between seawater and ocean rocks (Edmond et al., 1979; Stein and Stein, 1994; Elderfield and Schultz, 1996; Wheat et al., 2000). In particular, the discharge of hydrothermal fluid

in the deep ocean generates massive sulfide deposits. They also impact all oceanic geochemical cycles, including those of sulfur, iron and carbon (Amend et al., 2011; Hannington et al., 2011; German and Von Damm, 2006).

Life proliferates around black smokers. It is within the deep-sea sediments surrounding black smokers that the superphylum Asgard archaea was initially identified from metagenomic data and positioned as an archaeal ancestor of the eukaryotes (Spang et al., 2015; MacLeod et al., 2019; Weiss et al., 2016; Rodrigues-Oliveira et al., 2023; Eme et al., 2023). The unique microbial communities thriving in such a microhabitat, where hydrothermal fluids mix with seawater, stand apart from those found in the adjacent benthic zones (e.g. Cowen et al., 1986; Winn et al., 1986; Juniper et al., 1998; Dick and Tebo, 2010; Sheik et al., 2015).

However, the extent to which (hyper)thermophilic microorganisms colonize chimneys and their contribution to sulfide mineral formation remain open questions (Wirth, 2017; Hu et al., 2020; Baumgartner et al., 2022) despite the recent report of microorganisms entombed in minerals, especially pyrite, in the middle and outer layers of hydrothermal chimneys (Baumgartner et al., 2022). The middle and outer portions of a chimney wall are highly porous and likely permeable, which favours the mixing between reduced hydrothermal fluids and oxygenated seawater, thereby creating steep physicochemical gradients varying at small spatial scales (Tivey et al., 2002). Some authors have proposed that these layers harbour a population of hyperthermophilic microorganisms or at least that they could provide conditions suitable for their growth (Tivey et al., 2002; Schrenk et al., 2003; Lin et al., 2016). Supporting such scenarios, several studies reported the detection of biomarkers within chimney samples, such as the gene encoding 16S ribosomal RNA (Schrenk et al., 2003; Li et al., 2014) or bacterial and archaeal lipids (Blumenberg et al., 2007).

Mineral phases may also help to decipher whether or not microorganisms are biogeochemically active within chimneys. In fact, microbial activity may influence the dissolution and/or precipitation of hydrothermal minerals (e.g. Jannasch, 1995; Holden and Adams, 2003; Templeton et al., 2009; Houghton and Seyfried, 2010; Mansor et al., 2019; Meier et al., 2019) including pyrite, i.e. the most predominant sulfide of middle and outer layers (e.g. Lafitte et al., 1984; Rona et al., 1986; Langmuir et al., 1997; Grant et al., 2018). For instance, the metabolic activity of some hyperthermophilic, heterotrophic and S(0)-reducing archaea from the order Thermococcales, primarily isolated from hydrothermal marine vents, has been shown to induce the formation of greigite (Fe_3S_4) and of pyrite (FeS_2) when cultivated at 85 °C in an iron- and sulfur-rich synthetic medium simulating hydrothermal fluids (Gorlas et al., 2018; 2022; Truong et al., 2023). Laboratory experiments using Thermococcales have shown that the co-precipitated pyrite displays specific features, in particular a spherule shape with a diameter around 1 µm, a nanoscale texture with many ultra-small domains measuring 10 to 15 nm on average, and biogenic organic compounds in small but detectable quantities (Truong et al., 2023). These unique characteristics make them promising biosignatures to be searched for in extreme environments such as black smokers (Runge et al., 2022). Using them as biosignatures, determining whether such pyrite spherules occur in black smoker chimneys requires demonstrating that they clearly differ from the abiotic pyrite that is also found in the vicinity of hydrothermal vents. Here, we use elemental analyses (CHNS), X-ray diffraction (XRD), scanning and transmission electron microscopies (SEM and TEM), scanning transmission X-ray microscopy (STXM), and X-ray absorption near edge structure (XANES) spectroscopy to characterize the pyrite precipitates collected across the black smoker chimney (from the inner, hotter portion to the external, cooler portion) sampled at the Transatlantic Geotraverse Mound (TAG) site during the Bicose 2 mission (Cambon-Bonavita, 2018), documenting their shape, nanoscale texture and organic content. We then discuss the pertinence of particular pyrite spherules as biosignatures of living microorganisms within black smokers.

2 Materials and methods

2.1 The Trans-Atlantic Geotraverse hydrothermal site

The Transatlantic Geotraverse (TAG) site, at 26°08′ N on the Mid-Atlantic Ridge (MAR), is a mature vent field that has been active for ∼ 140 000 years (Lalou et al., 1993, 1995). It is located on the hanging wall of an active detachment fault at a 3600 m depth (Rona et al., 1986; Canales et al., 2007; deMartin et al., 2007). The chimneys lie along two concentric platforms that form a compound and elliptical mound with a 50 m high inner high-temperature mound and a 200 m wide outer low-temperature mound (Rona et al., 1993; Humphris and Kleinrock, 1996; White et al., 1998; Pontbriand and Sohn, 2014; Fig. 1a).

The inner high-temperature mound, produced by the hotter discharging fluid, is mainly composed of sulfides and to a lesser extent of sulfates, a few oxides, hydroxides and silicates (Rona et al., 1986, 1993). In contrast, the outer low-temperature mound and the surrounding sediment field are subjected to lower-temperature fluid discharges of lower-temperature fluids over extended periods. As a result, these latter locations are characterized by deposits of red Fe–Mn-rich amorphous iron oxides, Fe-silicates and other Mn–Fe-rich materials (Thompson et al., 1985, 1988; Lalou et al., 1986; Rona et al., 1993; Becker, 1996). The hydrothermal plumes proximal to chimneys are dominated by colloidal FeS aggregates (Yücel et al., 2021) and colloidal nanoparticles of euhedral pyrite (Rona et al., 1986; Yücel et al., 2011; Gartman et al., 2014) alongside Fe–C colloids (Baumgartner et al., 2023).

The TAG mound was the first hydrothermal vent to be discovered on the MAR during the 1972 and 1973 cruises

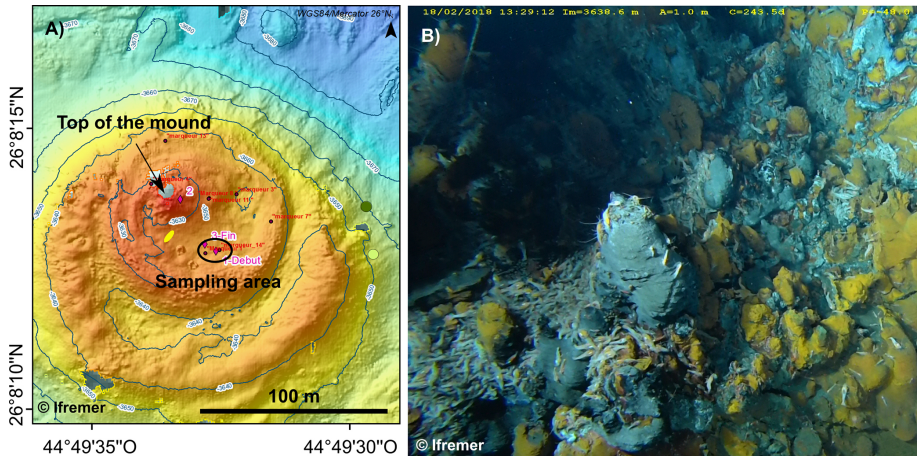

Figure 1. **(a)** Bathymetric map of the TAG site. The two concentric platforms appear in orange. The black arrow indicates the top of the mound and the dark ellipse indicates the sampling area. **(b)** Photograph of the area called the nursery-zone located in the inner caldera at the south-eastern base of the inner high-temperature mound. The abyssal shrimp photographed here belong to the genus *Rimicaris*.

by the National Oceanic and Atmospheric Administration (NOAA) TAG Project (Scott et al., 1974; Rona, 1980) and was eventually recognized as a presently active hydrothermal site comprising black smokers and massive sulfide mounds (Rona et al., 1984; Thompson et al., 1988; Beaulieu et al., 2015). In the last 10 years, four campaigns were conducted at the TAG hydrothermal field: Bicose 1 (Cambon-Bonavita, 2014), Hermine (Fouquet and Pelleter, 2017), Bicose 2 (Cambon-Bonavita, 2018) and Hermine 2 (Pelleter and Cathalot, 2022).

The sampling site of the present study is named the "nursery-zone" and is inhabited by abyssal shrimps belonging to the genus *Rimicaris* (Cambon-Bonavita, 2014; Konn et al., 2022). It was discovered during the Bicose 1 campaign and sampled during the Bicose 2 campaign. It occurs in an active area composed of tiny, recently formed black smokers, located in the inner caldera at the south-eastern base of the inner high-temperature mound (Fig. 1b).

2.2 Sample selection

For this study, we selected three samples from the same active chimney (labelled "Int", "Mid" and "Ext", respectively sampled from the internal, the middle and the external part of the chimney wall). The chimney, located at 26°8.223′ N–44°49.532′ W at a depth of 3640 m, was sampled on 4 February 2018 (Bicose 2 campaign, operation BIC2-PL01-01) by the Nautile submersible. The samples were placed in a collection box, brought to the surface and immediately stored in anaerobic flasks on board. The gas phase was replaced by N_2 to limit interaction with O_2. They were stored at 4 °C for 1 year, then the solid phase was vacuum-dried in an anoxic Jacomex™ glovebox under an N_2 atmosphere (< 1 ppm O_2). Dry samples were kept at 4 °C in sterile Eppendorf tubes before being analysed in the present study. For each analysis (CHNS analyses were conducted first), material (clamps, capsules, etc.) and surfaces were carefully cleaned with 70 % ethanol and handled with gloves and clamps to avoid contamination from external organic matter.

2.3 X-ray diffraction

Powdered samples (Ext, Mid and Int) were deposited on zero-background Si wafers and placed in a Spinner-configured bracket. XRD patterns were collected on a XPert Pro Panalytical™ diffractometer. Data were collected using Co $K\alpha$ radiation in continuous scan mode with an equivalent 0.03° 2θ step, counting 3 h per sample over the 5–90° 2θ range. Identification of mineral phases was made using EVA software and the PDF4 database: bianchite (PDF ID: 00-032-1478), marcasite (PDF ID: 00-037-0475), pyrite (PDF ID: 00-042-1340), sphalerite (PDF ID: 04-003-6940) and chalcopyrite (PDF ID: 01-074-1737) were identified.

2.4 Carbon, hydrogen, nitrogen and sulfur (CHNS) mass fraction: estimation of the elemental composition

Three fractions of each sample were weighed and measured to estimate their mean elemental composition. The tin containers in which the samples were weighed were handled with tweezers, cleaned with 70 % ethanol and dried between each weighing. Vanadium pentoxide (V_2O_5) was added as an oxidation catalyst to convert reduced sulfur phases into sulfur dioxide, thereby increasing the quality of total sulfur analysis. CHNS elemental data were collected with a Thermo Fischer Flash 2000 analyser, equipped with a He gas vector chromatograph column and a thermal conductivity detector (katharometer TCD). EAGER Xperience software was used to calculate the mass percentage of each element. A blank (an

empty tin capsule) was analysed at the start of the run, and the measured N, C and H values were subtracted from all sample measurements. The S value of the blank was below the detection limit. To ensure complete purging, the chromatographic column with carrier gas (He) was scanned for 2 min after the sulfur peak was registered.

2.5 Scanning electron microscopy coupled with energy dispersive X-ray spectroscopy (SEM-EDXS)

Powder samples (Ext, Mid and Int) were deposited on a carbon tape and were carbon coated. SEM-EDXS data were collected using a GEMINI ZEISS™ Ultra55 Field Emission Gun Scanning Electron Microscope on the MNHN PtME platform. This SEM is equipped with two Bruker™ XFlash silicon drift detectors in antagonist positions for EDXS. Both images and EDXS data were collected using an acceleration voltage of 15 kV at a working distance of 12.5 mm and 300 pA probe current.

2.6 Sample preparation by focused ion beam (FIB)

Ultrathin FIB sections (20 µm × 5 µm × 100 nm) were extracted from the samples prepared for SEM using a FEI Strata DB 235; NB – one cubic pyrite was isolated from the sample Int, one cubic pyrite aggregate was isolated from the sample Mid and two micrometric pyrite spherules were found in the sample Ext (namely Ext A and Ext B). Platinum strips were deposited prior to milling to strengthen the ultrathin sections. Milling at low gallium currents minimized artefacts such as the local gallium implantation, mixing of components, redeposition of the sputtered material on the sample surface and significant changes in the speciation of carbon-based polymers (Bernard et al., 2009; Schiffbauer and Xiao, 2009).

2.7 Transmission electron microscopy (TEM)

TEM data were collected using a JEOL JEM-2100F equipped with a field emission gun (FEG) operating at 200 kV in both TEM mode and scanning transmission mode (STEM). Minerals were identified using selected-area electron diffraction (SAED). Chemical maps were obtained in STEM mode using an EDXS system from JEOL (Si(Li) detector).

2.8 Scanning transmission X-ray microscopy and X-ray absorption near edge structure spectroscopy (STXM-XANES)

Analyses were performed on FIB foils to document the carbon speciation of the organic compounds present within the pyrite minerals using the HERMES STXM beamline at the Source optimisée de lumière d'énergie intermédiaire du LURE (SOLEIL) synchrotron (Saint-Aubin, France – Belkhou et al., 2015; Swaraj et al., 2017). X-ray absorption near edge structure (XANES) hypercube data (stacks) were collected with a spatial resolution of 100 nm at energy increments of 0.1 eV over the carbon (270–340 eV) absorption range with a dwell time of less than 1 ms per pixel to prevent irradiation damage (Wang et al., 2009). Energy calibration was made using the well-resolved 3p Rydberg peak of gaseous CO_2 at 294.96 eV for the C–K edge.

Stack alignments and extraction of XANES spectra were done using the Hyperspy Python-based package (De La Peña et al., 2018). Normalization of data was accomplished using the QUANTORXS freeware (Le Guillou et al., 2018). A parameter related to the concentration of C ($[C]_{STXM}$) was estimated from stacks collected at the C–K edge by normalizing the carbon quantity estimated from the spectra (following Le Guillou et al., 2018) to the absorption at 280 eV (i.e. below the carbon absorption edge). The value obtained is proportional to the true concentration of carbon, but the proportionality factor is experiment-dependent. Thus, the obtained $[C]_{STXM}$ values are regarded as qualitative. As a reference, the pyrite spherules produced in the presence of archaea (Truong et al., 2023) display a $[C]_{STXM}$ value of 4.65.

3 Results

3.1 X-ray diffraction

The X-ray diffractogram (Table S1 in the Supplement, Fig. 2) of Int reveals the presence of only pyrite (FeS_2) and chalcopyrite ($CuFeS_2$). An assemblage of marcasite (FeS_2), pyrite (FeS_2), sphalerite (ZnS) and chalcopyrite ($CuFeS_2$) is detected in Mid. An assemblage of marcasite (FeS_2), pyrite (FeS_2), sphalerite (ZnS), bianchite ($ZnSO_4$) and minor chalcopyrite ($CuFeS_2$) is detected in Ext.

3.2 CHNS elemental composition

CHNS elemental analyses confirm that each sample investigated is dominated by sulfur, compared to carbon and hydrogen (Fig. 3, Table S2). The sample Int contains 32.4(±0.05) wt % of S, the Mid sample 37.5(±0.09) wt % of S and the sample Ext 40(±0.09) wt % of S. Carbon content is lowest in Int (0.08(±0.02) wt %) compared to Mid 0.14(±0.02) wt % and Ext 0.21(±0.09) wt %. Similarly, the hydrogen content is 0.05(±0.04) wt % in Int, 0.05(±0.02) wt % in Mid and 0.08(±0.02) wt % in Ext. Nitrogen is generally below the detection limit.

3.3 Scanning electron microscopy

Pyrite and chalcopyrite are the main phases in Int, consistent with XRD data. Most pyrites in Int are cube-shaped crystals of about 50 µm in size (Fig. 4a) or aggregates of more than several hundreds of micrometres composed of cube-shaped crystals up to 80 µm in size (Fig. 4b). Octahedral-shaped pyrite is smaller, ranging from 2 to 10 µm in size (Fig. 4d). Int also contains chalcopyrite occurring as platelet-shaped sin-

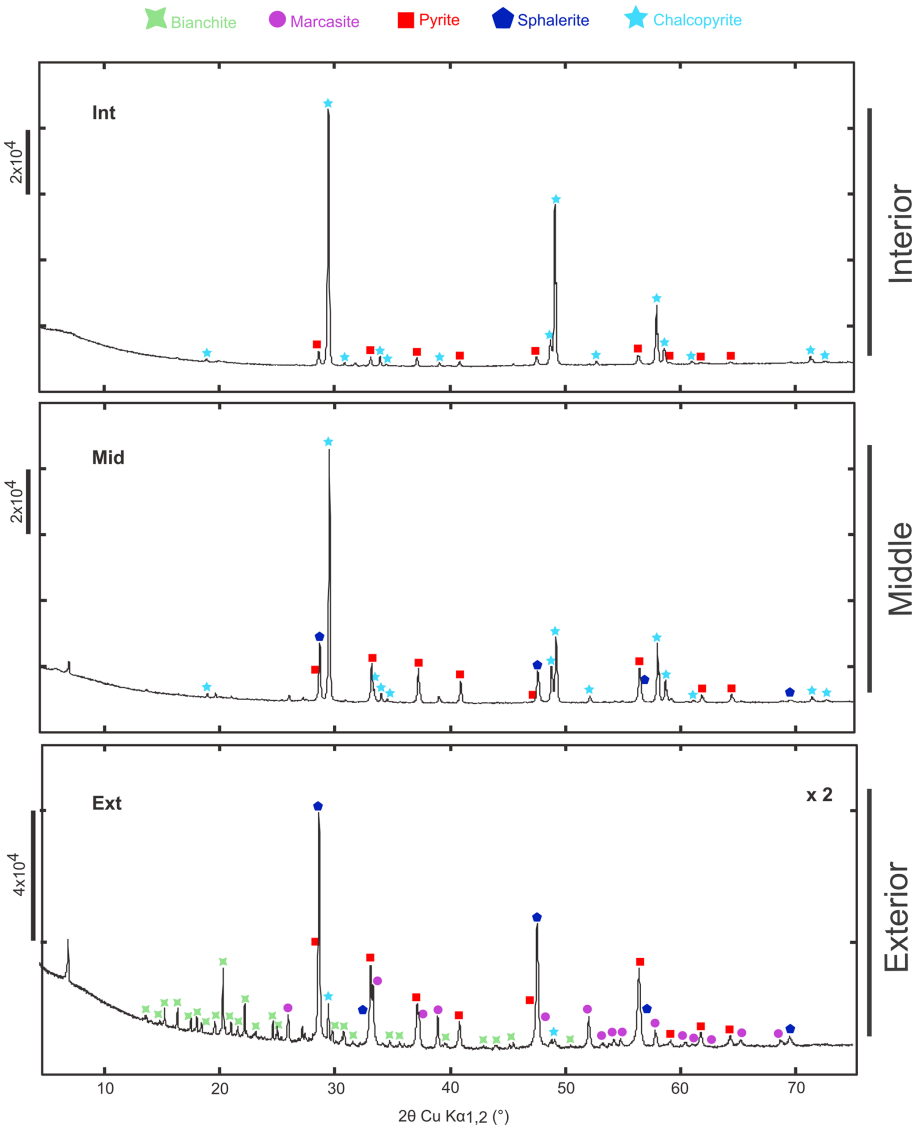

Figure 2. X-ray diffraction of TAG hydrothermal vent samples corresponding to different parts of the chimney's wall: internal (Int), middle (Mid) and external (Ext) portions. Each identified peak is labelled with bianchite (COD ID: 9014480; green cross), marcasite (COD ID: 1011013; purple circle), pyrite (COD ID: 9015842; red square), sphalerite (COD ID: 1538617; blue pentagon) and chalcopyrite (COD ID: 9015636; light-blue star). NB – the diffractogram of the Ext sample has been zoomed in by a factor of 2 for reasons of readability.

gle crystals of characteristic size ranging from 10 to 100 µm (Fig. 4c, d and e). Some Al-rich phyllosilicate can be associated with pyrite and chalcopyrite (Fig. 4d and e).

Various pyrite crystal morphologies are found in Mid, including aggregates measuring 50 µm and composed of irregular micrometric grains (Fig. 4f and g), as well as cubic and octahedral crystals ranging in size from 2 to 20 µm (Fig. 4h). Pyrite is also associated with quartz and silicates, in the form of grains ranging in size from 2 to 10 µm (Fig. 4f, g). Chalcopyrite also occurs as platelet-shaped crystals with characteristic sizes ranging from 10 to 50 µm (Fig. 4i).

In Ext, sphalerite is the predominant mineral phase and occurs as globular aggregates of hundreds of micrometres, composed of irregular micrometric grains (Fig. 4j–n). Pyrite is present as micrometric spherules with diameters of about 2 to 5 µm, with some of them trapped within sphalerite aggregates.

3.4 Transmission electron microscopy

As shown by TEM data collected on FIB foils, the cube-shaped pyrites of Int and Mid are massive single crystals (Fig. 5a, b, c, f, g and h) containing micrometric sphalerite inclusions, ranging in size from 800 nm to several micrometres (Figs. 5d, e, i and j and S1 in the Supplement). In contrast, the pyrite spherules of Ext (Fig. 6a and f) exhibit more complex

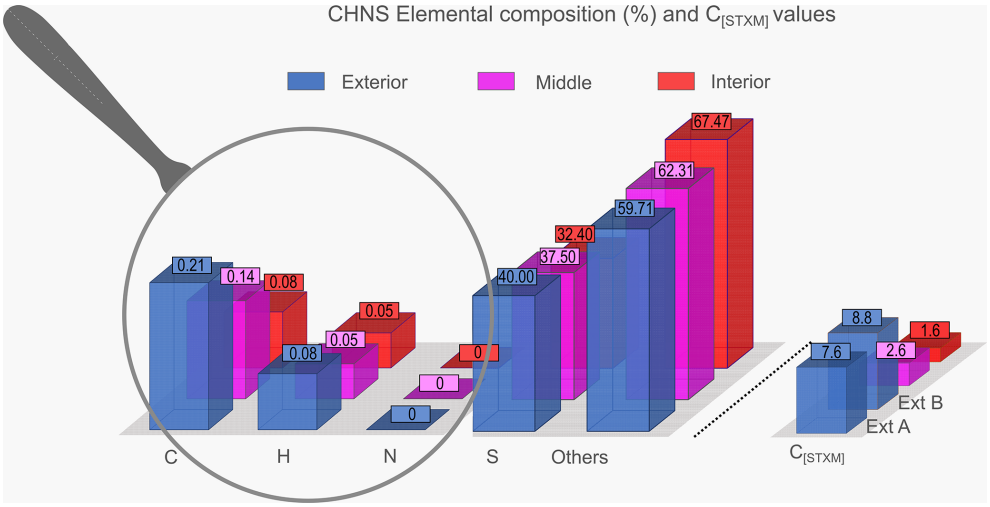

Figure 3. Elemental composition (C, H, N and S) and $C_{[STXM]}$ for Int (in red), Mid (in pink) and Ext (in blue). For the $C_{[STXM]}$ values, the Ext sample is divided into Ext A and Ext B (in blue).

nanoscale texture. The observed SAED patterns demonstrate that both spherules are single crystals (Fig. 6b, c, g and h), however, they are made up of a mosaic of slightly disoriented domains that never exceed a few hundred nanometres in size (Fig. 6d and e). TEM investigations and the SAED pattern of the sphalerite matrix revealed that it is composed of micrometric single crystals, measuring 1 to 2 micrometres (Fig. 6i, j and k). The sphalerite matrix crystals present evidence of dislocation (Fig. 6i), and the zebra patterns observed in Fig. 6j can be attributed to planar defects.

3.5 Scanning transmission X-ray microscopy and X-ray absorption near edge structure spectroscopy

Additional investigations using STXM and XANES spectroscopy reveal that the pyrite of Ext contains some carbon ($4.77 < [C]_{STXM} < 8.81$), i.e. at values even higher than that of pyrite spherules produced in the presence of archaea ($[C]_{STXM} = 4.65$ – Truong et al., 2023), while pyrite from Int and Mid exhibits lower $[C]_{STXM}$ values (1.55 and 2.62, respectively; Table S2). Of note, such $[C]_{STXM}$ values of the pyrites in each sample are correlated to the mass percentage of carbon detected by CHNS elemental analysis in the corresponding bulk sample, with the Int and Mid samples containing less carbon than the Ext sample (Fig. 3, Table S2).

The organic compounds detected in pyrite from Ext show a XANES spectrum with absorption features at 285.0, 286.5, 287.6, 288.5 and 290.5 eV attributed to aromatic rings or C=C olefinic bonds, C–S bonds, C–H bonds, C–C bonds and COOH groups, respectively (Bernard et al., 2009; Le Guillou et al., 2018). The asymmetry of the main feature at 288.5 eV may be related to the presence of amide groups absorbing at 288.2 eV. In contrast, the organic compounds detected in pyrite from Int show a XANES spectrum with almost no feature besides a very large one centred at about 288 eV attributed to CH bonds and a shoulder at 285 eV possibly attributed to aromatic rings or C=C olefinic bonds (Bernard et al., 2009; Le Guillou et al., 2018). The organic compounds detected in pyrite from Mid have a XANES spectrum with absorption features at 285.0, 286.5, 287.6, 288.5 and 290.5 eV attributed to aromatic rings or C=C olefinic bonds, C–S bonds, C–H bonds, C–C bonds and COOH groups, respectively (Bernard et al., 2009; Le Guillou et al., 2018). These absorption characteristics are similar to those of the Ext A and Ext B spectra, but the overall appearance of the spectrum is close to that of Int, with a broad dominance of aromatic and carboxylic groups.

4 Discussion

4.1 Textural variations along the temperature gradient

Sulfide assemblages as well as pyrite morphologies vary from the centre to the exterior of the chimney wall (Fig. 8). In the inner part of the structure (sample Int), the mineral assemblage consists almost exclusively of large platelets of chalcopyrite and cube-shaped pyrite of almost 100 µm in size (Figs. 2, 4a–c), which are typical of high-temperature settings > 300 °C (Haymon, 1983; Tivey and Delaney, 1986; Butler and Nesbitt, 1999). They are also typical of zone-refined sulfide, as fluids continually flow through the chimney (Wang et al., 2022). The exact nature of the phyllosilicates (Fig. 4) could not be determined; however, hydrothermal silicates are interesting markers of temperature and pH (Fulignati, 2020). Since aluminosilicate reactions at high temperatures produce and maintain the acidity on the hydrothermal fluid (Haymon and Kastner, 1986; Von Damm, 2001), the presence of Al-rich silicates (Fig. 4d and e) attests to direct contact with the fluid. The occurrence of octahedron-shaped pyrite crystals measuring 10 µm (Fig. 3d)

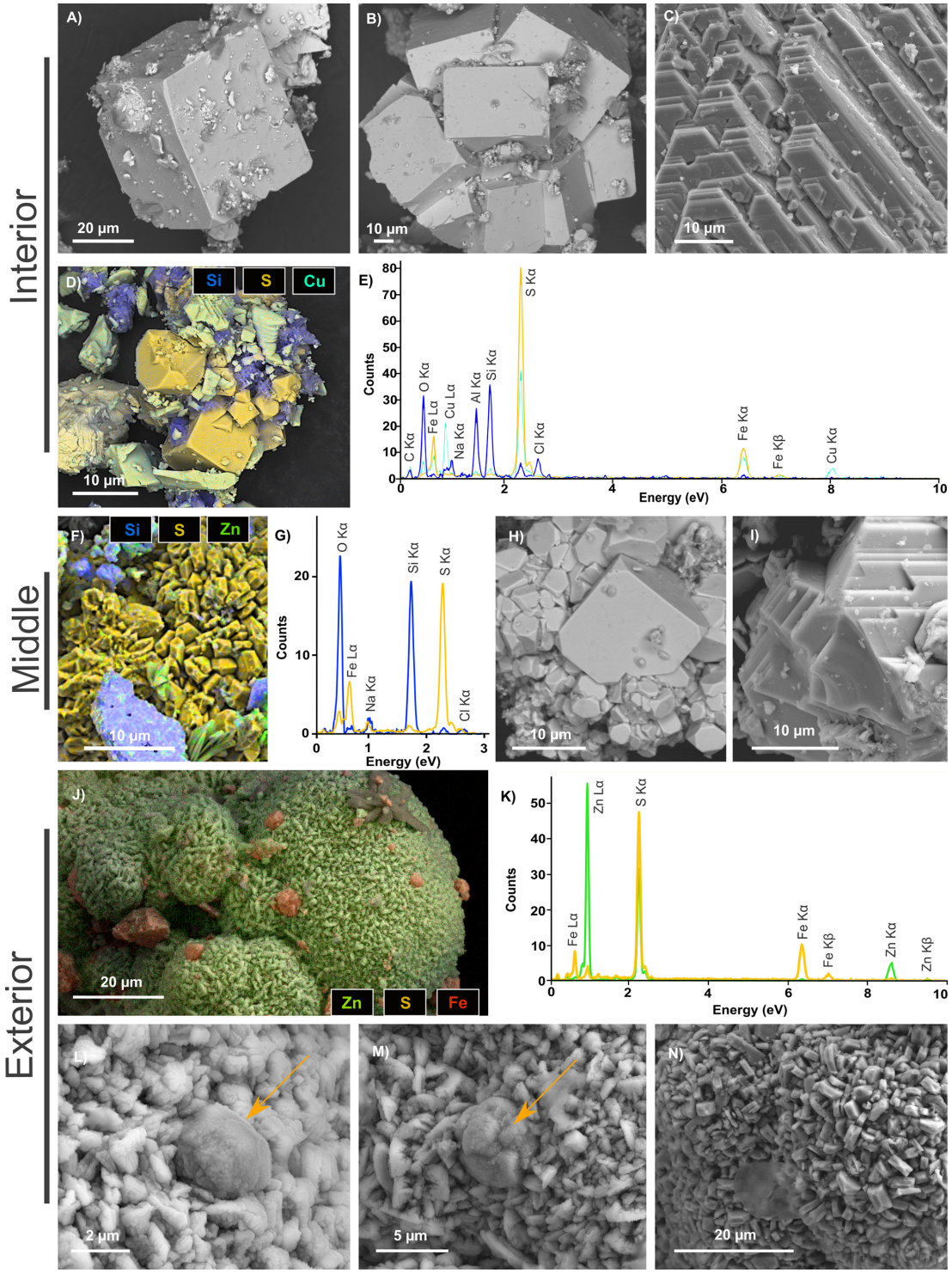

Figure 4. SEM investigations of pyrites from the chimney wall: **(a–e)** the inner part of the wall (Int), **(f–i)** the middle part of the wall (Mid) and **(j–n)** the external part of the wall (Ext). **(a)** Cubic pyrite crystal. **(b)** Aggregates of euhedral pyrite crystals. **(c)** Platelet-shaped chalcopyrite crystals. **(d–e)** EDXS chemical map of an aggregate of pyrites (in yellow), chalcopyrites (in light green) and phyllosilicates (in blue) and corresponding EDXS spectra. **(f–g)** EDXS chemical map of an aggregate of pyrites (in yellow) associated with silicates (in blue) and the associated EDXS spectra using the same colour code. **(h)** Aggregates of euhedral single crystals of pyrite with a large distribution in sizes and facies. **(i)** Platelet-shaped chalcopyrite single crystals. **(j–k)** EDXS chemical map of a rounded sphalerite aggregate (in green) with small pyrites (in orange) from the Ext sample and associated EDXS spectra using the same colour code. **(l–m)** Micrometric pyrite spherules (orange arrow) trapped in a sphalerite matrix in the Ext sample. **(n)** Focus on the sphalerite matrix, composed of irregular micrometric grains.

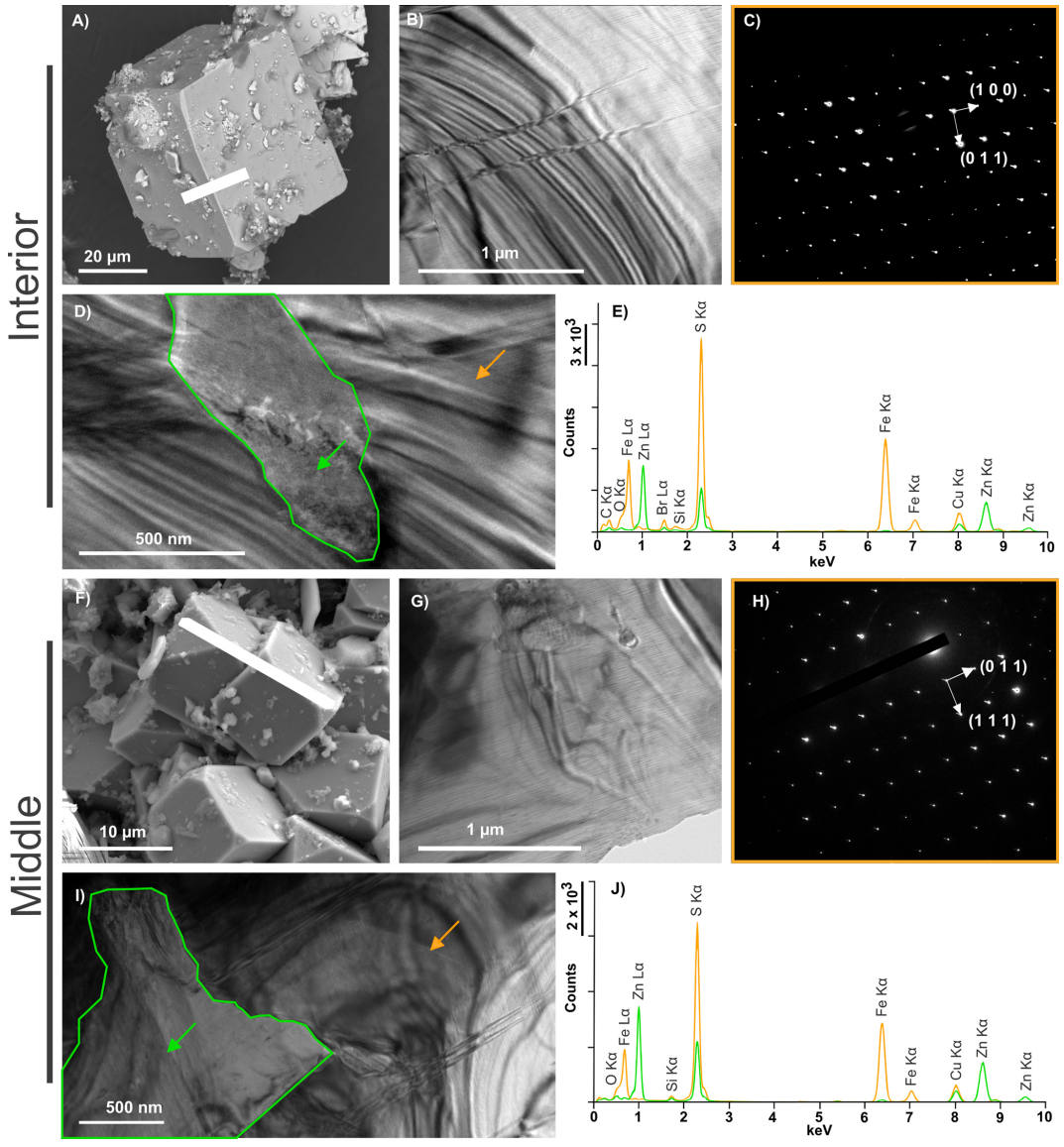

Figure 5. TEM characterization of FIB sections of pyrite detected in Int **(a–e)** and Mid **(f–j)**. **(a)** SEM image showing the location of the Int FIB section. **(b)** TEM overview of the Int FIB section and **(c)** associated SAED pattern revealing that the entire FIB section corresponds to a single cubic crystal of pyrite (zone axis [0$\bar{1}$1]). **(d)** Micrometric ZnS inclusion (green arrow) in pyrite (orange arrow). **(e)** EDXS spectra of the zones highlighted by the arrows. **(f)** SEM image showing the location of the Mid FIB section. **(g)** TEM overview of the Mid FIB section and **(h)** associated SAED revealing that the entire FIB section corresponds to a single cubic crystal of pyrite (zone axis [01$\bar{1}$]). **(i)** Micrometric ZnS inclusion (green arrow) in pyrite (orange arrow). **(j)** EDXS spectra of the zones highlighted by the arrows.

and the close associations between pyrites and individual fine-grained particles of sphalerite (Fig. 5d and e) also indicate precipitation at high temperatures (> 250 °C) (Rona et al., 1986; Murowchick and Barnes, 1987). Overall, these mineral associations are consistent with high-temperature hydrothermal fluid discharge at the centre of hydrothermal chimneys.

In the middle section of the chimney wall (sample Mid), sphalerite is present in higher concentrations, as shown by its detection using XRD, together with the presence of pyrite and chalcopyrite (Figs. 2, 8). This is consistent with previous observations of abundant Zn-rich phases occurring within the porous portions of chimney walls, whereas the hotter centres of such chimneys are typically Cu-rich (chalcopyrite; Rona et al., 1986; Fouquet et al., 1996; Hu et al., 2020; Baumgartner et al., 2022). The presence of some micrometric sphalerite occurring as inclusions within cube-shaped crystals of pyrite (Fig. 5i and j) attests to the probability that at least some of the sphalerite crystals have precipitated at high temperatures (> 250 °C; Murowchick and Barnes, 1987; Hu et al., 2019),

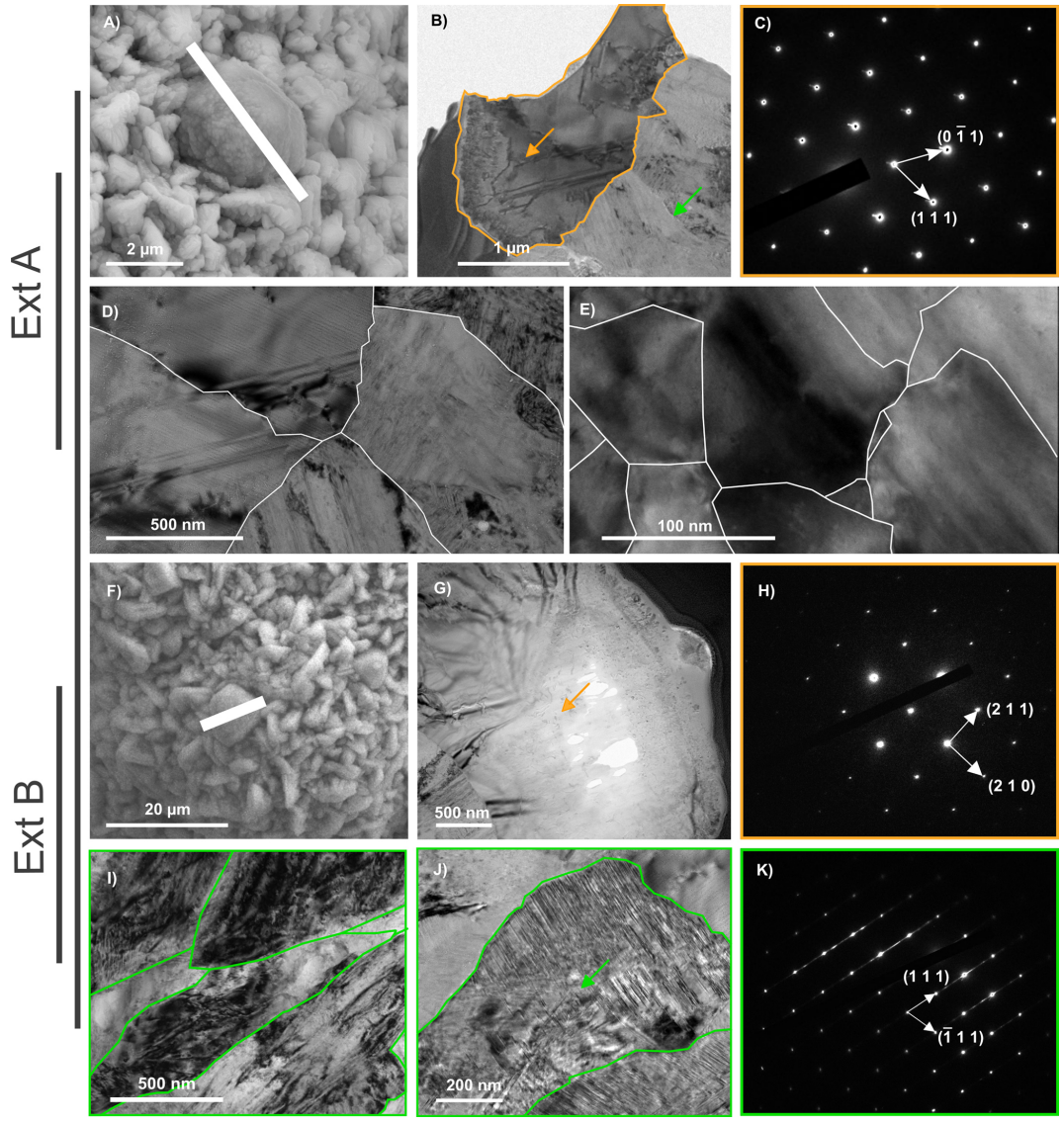

Figure 6. TEM characterization of two FIB sections of pyrite spherules isolated from Ext (Ext A and Ext B). **(a)** SEM image showing the location of the Ext A FIB section. **(b)** TEM image of the Ext A FIB section showing the pyrite spherule (orange arrow) entrapped in the sphalerite matrix (green arrow) and **(c)** associated pyrite SAED pattern revealing that the spherule consists of a single crystal (zone axis $[2\bar{1}\bar{1}]$). **(d–e)** TEM images of sub-grain boundaries (in white) within the single pyrite crystal. **(f)** SEM image showing the location of the Ext B FIB section. **(g)** TEM image of the Ext B FIB section showing the pyrite spherule (orange arrow) and **(h)** associated SAED pattern revealing that the spherule consists of a single crystal (zone axis $[1\bar{2}0]$). **(i–j)** TEM images of the sphalerite matrix composed of a number of micrometric crystals (grain boundaries in green). **(k)** SAED pattern of the single sphalerite crystal shown in **(j)** (zone axis $[0\bar{2}2]$).

as is the case for the micrometric sphalerite crystals from Int. Although more porous than the innermost part of the chimney and thus more exposed to mixing with seawater, the middle part of the chimney is still likely exposed to intermittent high temperatures.

In the external part of the chimney wall (sample Ext), sulfates such as bianchite and iron oxides were identified in addition to pyrite, sphalerite and chalcopyrite (Figs. 2, 8). These mineral phases are typical products of low-temperature alteration of sulfides. This is especially the case with bianchite, which has already been described in inactive sulfide mounds and at the interface between the chimney wall and the seawater (Hekinian et al., 1980; Lafitte et al., 1984). Still, the presence of globular assemblages of about 100 µm made of micrometric-sized pyrite spherules and sphalerite (Figs. 5j to n, 6i to k and 8) shows that the outermost part of the chimney wall has also been affected by hydrothermal fluid discharges. The fine-grained particles of the sphalerite clusters are likely to have formed in conditions where the nucleation rate is greater than the growth rate,

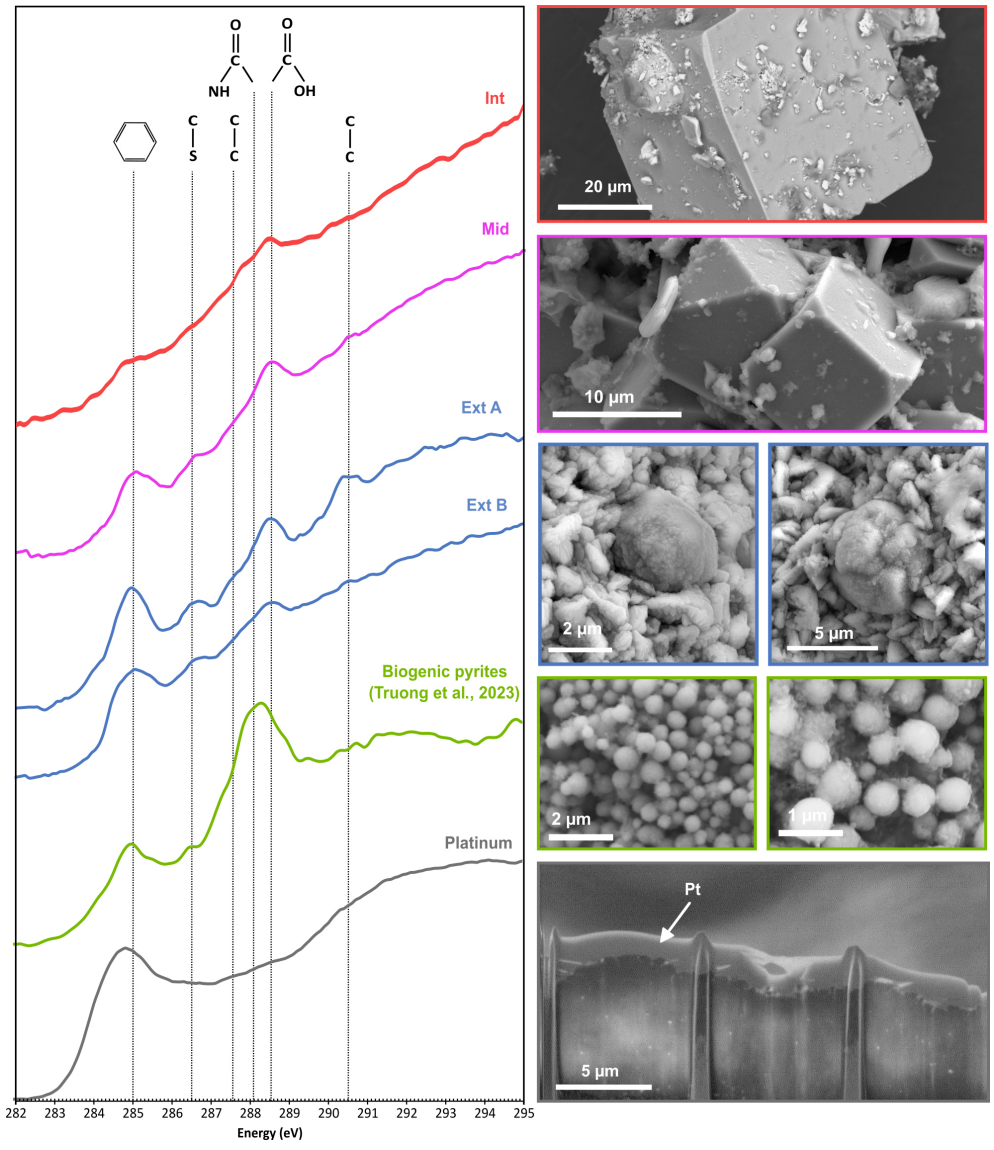

Figure 7. XANES spectra at the carbon–K edge (left) of the organic compounds detected in pyrites from the samples investigated in this study (Int, Mid, Ext A and Ext B) and SEM images of these pyrites (right). Furthermore, the spectrum of the organic compounds detected in spherules of pyrite produced in the presence of Thermococcales (labelled Biogenic pyrites) and SEM images of these pyrites (Truong et al., 2023) are shown for comparison. The spectrum of the organo-metal used to protect the FIB sections during preparation serves as a reference (marked "Platinum"). Absorption features at 285.0, 286.4, 287.6, 288.1, 288.5 and 290.5 eV are attributed to C=C bonds, C–S bonds, C–H bonds, C–N bonds (amide groups), COOH (carboxylic groups) and C–C bonds, respectively.

i.e. during the initial mixing of the hot acidic venting fluids (250 to 300 °C) with the seawater (4 °C) (Hu et al., 2019). Such a microtexture of sphalerite indicates a rapid precipitation in response to strong physicochemical gradients in the porous outer wall (Tivey, 1995; Hu et al., 2019). Every sphalerite crystal presents evidence of dislocation (Fig. 6i), likely caused by rapid cooling or by dynamic recrystallization (Cugerone et al., 2024). Planar defects have also been observed on single crystals of sphalerite (Fig. 6j), possibly accommodating excesses in iron and oxygen (Šrot et al., 2003; Xu et al., 2016) or simply created by steep physicochemical gradients of either temperature or oxygen as a result of direct contact with seawater. This suggests that the outer chimney wall experienced significant temperature variations from elevated temperatures, although generally 250 °C down to 2 °C, the inferred temperature of deep-ocean seawater.

Altogether, the variations in nature, size and shape of sulfide minerals from the inner to the outer part of the chimney wall inform us about the temperature gradient across the chimney wall, from very elevated temperatures in the inner part (> 250 °C) to very low temperatures in the outer part (close to 2 °C). This is consistent with pre-

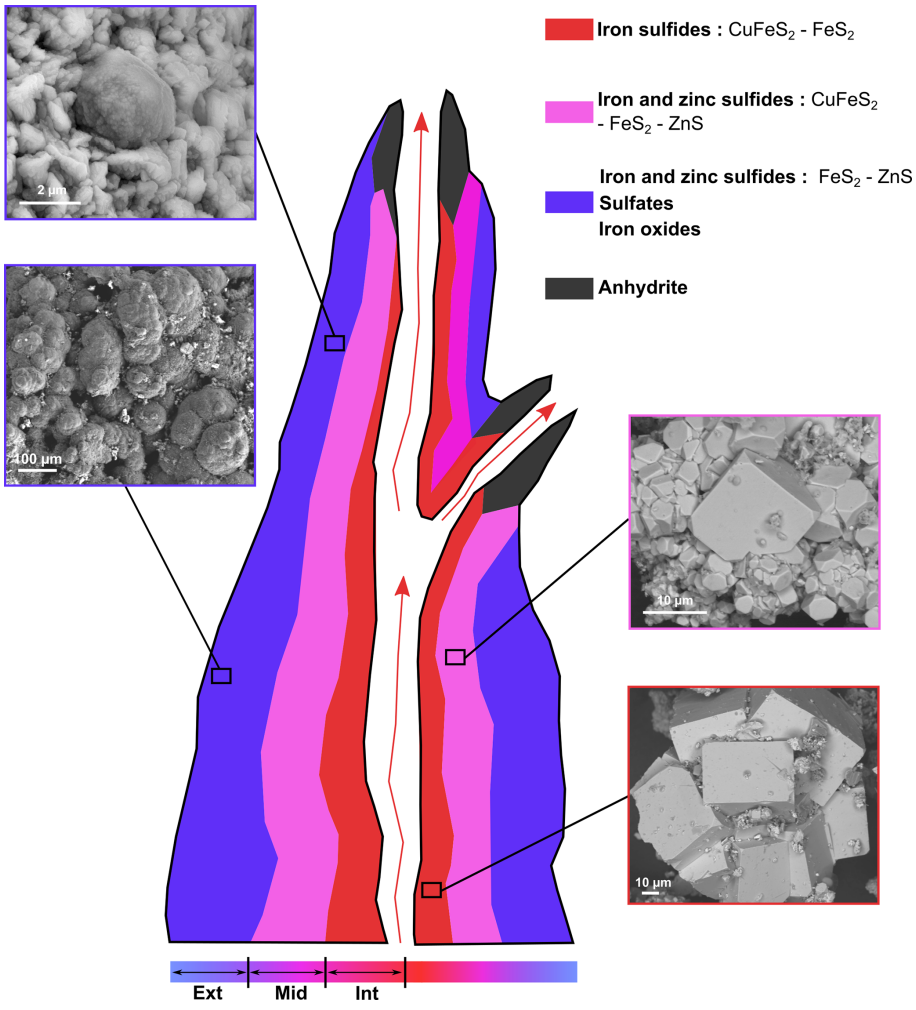

Figure 8. Schematic longitudinal transect of a hydrothermal vent showing the sulfide assemblages and pyrite morphologies at different locations within the chimney wall (not to scale).

vious studies, where euhedral crystals are found to precipitate at temperatures above and around 250 °C, conditioned by surface-controlled growth, while dendritic crystals precipitate at lower temperature, conditioned by diffusion-controlled growth (Murowchick and Barnes, 1987).

4.2 Identification of traces of life in the chimney wall

Obviously, the inner part of the chimney, in direct contact with the hot (> 300 °C) hydrothermal fluid, cannot support life. To date, the highest temperature withstood by hyperthermophilic microorganisms is 122 °C under 40 MPa hydrostatic pressure (*Methanopyrus kandleri* – Takai et al., 2008). In the present study, carbon and hydrogen were, however, detected in Int (Fig. 3, Table S2). The carbon speciation in this organic material is consistent with hydrocarbons (Fig. 7), which could be either abiotic or biogenic. In fact, such hydrocarbons could have been produced by the thermal cracking of (biogenic) organic materials that had been transported from the external parts of the chimney. But similar hydrocarbons could have been abiotically produced within or beneath the hydrothermal vent via Fischer–Tropsch-like processes (e.g. Simoneit, 1993; Kvenvolden and Simoneit, 1990; Cruse et al., 2006; McCollom and Seewald, 2007; McCollom et al., 2010) or via other CO_2-reduction processes (Heinen and Lauwers, 1996; Vladimirov et al., 2004). Regardless, even when assuming a biological origin for the associated organic carbon, biological controls on the formation of the inner pyrite are ruled out given its presence in the uninhabitable chimney centre, where high crystallization temperatures contributed to its consistently macrocrystalline, euhedral form. The pyrite spherules found in the external parts of the chimney require more discussion. The pyrite spherules exhibit morphologies, microtextures and organic contents similar to pyrite spherules produced by (or at least in the presence of) hyperthermophilic archaea such as Thermococcales. Relying on cultures of *Thermococcus kodakarensis*, Truong et al. (2023) reported the production of

very similar pyrite spherules of about 1 µm in diameter composed of nanocrystalline domains, resulting in a smooth surface texture at the spherule scale. Pyrite from Ext also shows a spherule shape, albeit with larger sizes of about 2 to 5 µm (Fig. 4l, m and n). The spherules are made of an assemblage of smaller crystallographically coherent domains delimited by annealed sub-grain boundaries (Fig. 6d). Such a microtexture could result from the recrystallization and Ostwald ripening upon thermal annealing of an assemblage of smaller spherules containing much smaller initial domains (e.g. Li et al., 2013; Nielsen et al., 2014; De Yoreo et al., 2015). Moreover, STXM-XANES investigations revealed that the pyrite spherules in Ext contain a relatively high concentration of organic compounds with aromatic rings or C=C bonds, C–S bonds, C–H bonds, C–C bonds, COOH groups and possibly amide groups (Fig. 7): i.e. organic compounds with a chemical structure consistent with the thermal maturation of the organic compounds found in the biogenic pyrite spherules produced in the presence of *Thermococcus kodakarensis* (Truong et al., 2023). Altogether, the pyrite spherules from Ext could be a thermally matured version of biogenic pyrite spherules similar to those made by Thermococcales, i.e. indirectly influenced by microbial activity, as reported by Truong et al. (2023). This still has to be demonstrated experimentally, but if true, the occurrence of these pyrite spherules would indicate colonization of chimneys of black smokers by thermophilic or hyperthermophilic microorganisms, their presence contributing to mineral formation in the chimneys. This would be in line with previous suggestions based on laboratory experiments (Wirth et al., 2017, 2018) as well as with the recent report of possible biofilms of coccoid microorganisms entombed within pyrite in the outer zone of a similar chimney (Baumgartner et al., 2022). This would demonstrate that despite steep physicochemical gradients responsible for recrystallization episodes at higher temperatures and rapid cooling, the external parts of the chimneys of black smokers are both habitable and (during at least at some time periods) inhabited.

Still, it remains to demonstrate that these pyrite spherules are true biosignatures, i.e. that similar spherules cannot be produced abiotically. In the presence of Thermococcales, the production of pyrite spherules directly results from their metabolism responsible for the conversion of sulfur into polysulfides and/or even more reactive colloidal sulfur, which reacts with ferrous sulfide (FeS) to form pyrite spherules (Gorlas et al., 2015, 2022; Truong et al., 2023). However, in natural settings such as chimneys and plumes of black smokers, even though the proportion of nanoparticulate sulfur is not negligible – nanoparticles of elemental sulfur can account for up to 44 % of the total sulfur present in the plumes of the Mid-Atlantic Ridge (Findlay et al., 2014) – colloidal sulfur is not necessarily related to microbial activity (Findlay, 2016), and polysulfides resulting from reactions between elemental sulfur and sulfide ions (Schwarzenbach and Fischer, 1960) or from the oxidation of sulfides by oxygen (Luther et al., 1986; Steudel, 1996) are also present. Pyrite spherules may thus form in black smoker chimneys in the absence of microorganisms, as is the case in the internal portions of the chimneys where massive pyrite was found. The mosaic microtexture of pyrite spherules can be interpreted in two ways. On the one hand, rapid nucleation associated with a low growth rate, similar to that observed in framboidal pyrite, could produce such a microtexture. The association of pyrite spherules with globular sphalerite clusters made up of fine-grained particles would be an argument in favour of rapid precipitation at temperatures well above the life limit of hyperthermophilic microorganisms. On the other hand, organic matter creates favourable conditions for the formation of microcrystalline domains. The presence of organic matter at sub-grain boundaries (Fig. 7) can prevent the recrystallization of the submicrometric crystallographically coherent domains into bigger single crystals, as is the case for the biogenic pyrite spherules produced in cultures (Truong et al., 2023). Still, although it has been shown that cellular compounds can be trapped preferentially in iron sulfides (Nabeh et al., 2022) and although the organic material detected within the pyrite spherules from Ext is consistent with biogenic organic compounds that had experienced thermal maturation, an abiotic origin remains equally likely given the lack of concrete evidence for biological influences. In fact, the specificities of pyrite produced via abiotic processes in the presence of various organic compounds and under hydrothermal conditions remain to be constrained experimentally. As such, for the time being, the pyrite spherules reported here should only be regarded as possible biosignatures.

Finally, the cubic pyrite from Mid contains more organic compounds than that from Int, although significantly less than the pyrite spherules in Ext. Moreover, these organic compounds are chemically consistent with a mixture of the compounds detected in the cube-shaped pyrite from Int with those detected in the pyrite spherules from Ext. This is puzzling, since the portions from which Int and Ext have been sampled are very different in terms of temperature conditions. A possible explanation involves transport of (and possible reactions between) organic compounds produced in the innermost part (likely via abiotic processes or thermal cracking of organic matter) and organic compounds produced in the outermost part (likely by life) within the porosity of the permeable chimney wall (Tivey et al., 2002; Zhu et al., 2007). This suggests that the different portions of the chimney wall are not isolated from one another and that depending on the temperature, hyperthermophilic microorganisms or their remnants have the potential to be detected in a significant fraction of the chimney wall beyond their growth location.

5 Conclusions

The study of hydrothermal pyrite encompassing both inner and outer portions of a black smoker chimney wall down to the nanometre scale is a promising technique to implement in the search for hyperthermophilic biosignatures. The identification of pyrite spherules sharing similarities with pyrite spherules produced in the laboratory in the presence of hyperthermophilic archaea suggests that the external part of the chimney wall investigated here is (or at least has been) inhabited by microorganisms that contributed to the mineral production.

Obviously, additional information must be obtained to undoubtedly confirm that these pyrite spherules can be used as biosignatures. In this regard, a sulfur isotope study is envisioned as the next step. Organic matter was detected in isolated pyrite from each part of the chimney wall, presenting quite distinct organic compounds between the inner and outer parts of the chimney wall, despite signs of thermal maturation in both cases. Thermal ageing experiments should be carried out to document the morphological, microtextural and chemical evolution of biogenic pyrite spherules produced in the laboratory in order to provide solid constraints to aid their identification in natural environments and to help determine the biological origin of organic compounds detected in natural pyrites. Also, isotopic measurements could and/or should be performed, as the sulfur-rich minerals produced by (or in the presence of) life generally exhibit peculiar sulfur isotope compositions (e.g. Marin-Carbonne et al., 2018, 2020, 2022) and/or iron isotope compositions (Boyce et al., 1993; Mansor, 2017). Furthermore, laboratory experiments have to be conducted under abiotic conditions (i.e. in the absence of life) to determine whether or not similar pyrites could form in the absence of life.

Although much work remains to be done, there is no doubt that combining the fine-scale mineralogical characterization of chimneys and perfectly controlled laboratory experiments will contribute to providing of a solid base to support further biological exploration of black smokers.

Data availability. The original contributions presented in this study are included in the article/Supplement; further inquiries can be directed to the corresponding author.

Supplement. The supplement related to this article is available online at: https://doi.org/10.5194/ejm-36-813-2024-supplement.

Author contributions. CT, SB, AG and FG contributed to the conceptualization and design of the study. CT and AG conducted the powder X-ray diffraction. CT and FG conducted the electron microscopy analyses. FB conducted the CHNS elemental analyses. CT and SB conducted the STXM-XANES analyses. CT wrote the first draft of the paper. CT, SB, FG, AG and FB wrote the sections of the paper. All authors contributed to the paper revision and read and approved the submitted version.

Competing interests. The contact author has declared that none of the authors has any competing interests.

Disclaimer. Publisher's note: Copernicus Publications remains neutral with regard to jurisdictional claims made in the text, published maps, institutional affiliations, or any other geographical representation in this paper. While Copernicus Publications makes every effort to include appropriate place names, the final responsibility lies with the authors.

Acknowledgements. We acknowledge the support of the Bicose 2 campaign (IFREMER), of the IMPMC-MNHN microscopy platform, of the IMPMC X-ray diffraction platform and of the SOLEIL HERMES beamline. We thank Erwan Roussel and Marie-Anne Cambon-Bonavita (IFREMER) for providing us the valuable samples from the Bicose 2 campaign, Mike Russel and Wolfgang Nitschke for their thorough revision of the manuscript, Elisabeth Malassis (IMPMC) for her administrative support, Sylvain Pont (IMPMC) for his help with SEM-EDXS, Jean-Michel Guigner (IMPMC) for his help with TEM, Ludovic Delbes (IMPMC) for his help with XRD, David Troadec (IEMN) for the preparation of the FIB sections, Corentin Le Guillou (UMET) for his help with STXM and Stefan Stanescu for his expert support of the HERMES beamline at SOLEIL.

Financial support. This research has been supported by the Muséum National d'Histoire Naturelle (MNHN), Sorbonne-Université (SU), Agence Nationale de la Recherche (ANR), project HYPERBIOMIN (grant no. ANR-20-CE02-0001-01).

Review statement. This paper was edited by Elena Belluso and reviewed by two anonymous referees.

References

Amend, J. P., McCollom, T. M., Hentscher, M., and Bach, W.: Catabolic and anabolic energy for chemolithoautotrophs in deep-sea hydrothermal systems hosted in different rock types, Geochim. Cosmochim. Ac., 75, 5736–5748, https://doi.org/10.1016/j.gca.2011.07.041, 2011.

Baumgartner, R. J., Hu, S., Van Kranendonk, M. J., and Verrall, M.: Taphonomy of microorganisms and microbial microtextures at sulfidic hydrothermal vents: A case study from the Roman Ruins black smokers, Eastern Manus Basin, Geobiology, 20, 479–497, https://doi.org/10.1111/gbi.12490, 2022.

Baumgartner, R. J., Teece, B. L., Rasmussen, B., Muhling, J., Rickard, W. D., Pejcic, B., Hu, S., Bourdet, J., Caruso, S., Van Kranendonk, M. J., and Grice, K.: Exceptional preservation of organic matter and iron-organic colloidal mineralization in hydrothermal black smoker-type sulfide mineralization

from the Paleoarchean seafloor, Chem. Geol., 618, 121296, https://doi.org/10.1016/j.chemgeo.2022.121296, 2023.

Beaulieu, S. E., Baker, E. T., and German, C. R.: Where are the undiscovered hydrothermal vents on oceanic spreading ridges?, Deep-Sea Res. Pt. II, 121, 202–212, https://doi.org/10.1016/j.dsr2.2015.05.001, 2015.

Becker, K.: Pre-drilling observations of conductive heat flow at the TAG active mound using DSV Alvin, Proc. ODP. Init. Repts, 158, 23–29, 1996.

Belkhou, R., Stanescu, S., Swaraj, S., Besson, A., Ledoux, M., Hajlaoui, M., and Dalle, D.: HERMES: a soft X-ray beamline dedicated to X-ray microscopy, J. Synchrotron. Radiat., 22, 968–979, https://doi.org/10.1107/S1600577515007778, 2015.

Bernard, S., Benzerara, K., Beyssac, O., Brown Jr., G. E., Stamm, L. G., and Duringer, P.: Ultrastructural and chemical study of modern and fossil sporoderms by Scanning Transmission X-ray Microscopy (STXM), Rev. Palaeobot. Palyno., 156, 248–261, https://doi.org/10.1016/j.revpalbo.2008.09.002, 2009.

Blumenberg, M., Seifert, R., Petersen, S., and Michaelis, W.: Biosignatures present in a hydrothermal massive sulfide from the mid-Atlantic ridge, Geobiology, 5, 435–450, https://doi.org/10.1111/j.1472-4669.2007.00126.x, 2007.

Boyce, A. J., Coleman, M. L., and Russell, M. J.: Formation of fossil hydrothermal chimneys and mounds from Silvermines, Ireland, Nature, 306, 545–550, https://doi.org/10.1038/306545a0, 1983.

Butler, I. B. and Nesbitt, R. W.: Trace element distributions in the chalcopyrite wall of a black smoker chimney: insights from laser ablation inductively coupled plasma mass spectrometry (LA–ICP–MS), Earth Planet. Sc. Lett., 167, 335–345, https://doi.org/10.1016/S0012-821X(99)00038-2, 1999.

Cambon-Bonavita, M.-A.: BICOSE cruise, RV Pourquoi pas?, French Oceanographic Cruises, https://doi.org/10.17600/14000100, 2014.

Cambon-Bonavita, M.-A.:BICOSE 2 cruise, RV Pourquoi pas?, French Oceanographic Cruises, https://doi.org/10.17600/18000004, 2018.

Canales, J. P., Sohn, R. A., and Demartin, B. J.: Crustal structure of the Trans-Atlantic Geotraverse (TAG) segment (Mid-Atlantic Ridge, 26° 10′ N): Implications for the nature of hydrothermal circulation and detachment faulting at slow spreading ridges, Geochem. Geophy. Geosy., 8, 1–18, https://doi.org/10.1029/2007GC001629, 2007.

Corliss, J. B., Dymond, J., Gordon, L. I., Edmond, J. M., von Herzen, R. P., Ballard, R. D., Green, K., Williams, D., Bainbridge, A., Crane, K., and van Andel, T. H.: Submarine thermal springs on the Galapagos Rift, Science, 203, 1073–1083, https://doi.org/10.1126/science.203.4385.1073, 1979.

Cowen, J. P., Massoth, G. J., and Baker, E. T: Bacterial scavenging of Mn and Fe in a mid-to far-field hydrothermal particle plume, Nature, 322, 169–171, https://doi.org/10.1038/322169a0, 1986.

Cruse, A. M. and Seewald, J. S.: Geochemistry of low-molecular weight hydrocarbons in hydrothermal fluids from Middle Valley, northern Juan de Fuca Ridge, Geochi. Cosmochim. Ac., 70, 2073–2092, https://doi.org/10.1016/j.gca.2006.01.015, 2006.

Cugerone, A., Oliot, E., Munoz, M., Barou, F., Motto-Ros, V., and Cenki, B.: Plastic deformation and trace element mobility in sphalerite, Am. Mineral., in press, https://doi.org/10.2138/am-2023-9215, 2024.

De la Peña, F., Ostasevicius, T., Fauske, V. T., Burdet, P., Prestat, E., Jokubauskas, P., Nord, M., MacArthur, K. E., Sarahan, M., Johnstone, D. N., Taillon, J., Eljarrat, A., Migunov, V., Caron, J., Furnival, T., Mazzucco, S., Aarholt, T., Walls, M., Slater, T., Winkler, F., Martineau, B., Donval, G., McLeod, R., Hoglund, E. R., Alxneit, I., Hjorth, I., Henninen, T., Zagonel, L. F., and Garmannslund, A.: hyperspy/hyperspy: HyperSpy 1.3, Zenodo, https://doi.org/10.5281/zenodo.583693, 2018.

Demartin, B. J., Sohn, R. A., Pablo Canales, J., and Humphris, S. E.: Kinematics and geometry of active detachment faulting beneath the Trans-Atlantic Geotraverse (TAG) hydrothermal field on the Mid-Atlantic Ridge, Geology, 35, 711–714, https://doi.org/10.1130/G23718A.1, 2007.

De Yoreo, J. J., Gilbert, P., Sommerdijk, N., Penn, L., Whitelam, S., Joester, D., Zhang, H., Rimer, J., Narvotsky, A., Banfield, J., Wallace, A., Michel, M., Meldrum, F., Cölfen, H., and Dove, P.: Crystallization by particle attachment in synthetic, biogenic, and geologic environments, Science, 349, 498–508, https://doi.org/10.1126/science.aaa6760, 2015.

Dick, G. J. and Tebo, B. M.: Microbial diversity and biogeochemistry of the Guaymas Basin deep-sea hydrothermal plume, Environ. Microbiol., 12, 1334–1347, https://doi.org/10.1111/j.1462-2920.2010.02177.x, 2010.

Edmond, J. M., Measures, C., McDuff, R. E., Chan, L. H., Collier, R., Grant, B., Gordon, L. I., and Corliss, J. B.: Ridge crest hydrothermal activity and the balances of the major and minor elements in the ocean: The Galapagos data, Earth Planet. Sc. Lett., 46, 1–18, https://doi.org/10.1016/0012-821X(79)90061-X, 1979.

Elderfield, H. and Schultz, A.: Mid-ocean ridge hydrothermal fluxes and the chemical composition of the ocean, Annu. Rev. Earth Planet. Sc., 24, 191–224, https://doi.org/10.1146/annurev.earth.24.1.191, 1996.

Eme, L., Tamarit, D., Caceres, E. F., Stairs, C. W., De Anda, V., Schon, M. E., Seitz, K. W., Dombrowski, N., Lewis, W. H., Homa, F., Saw, J. H., Lombard, J., Nunoura, T., Li, W.-J., Hua, Z.-S., Chen, L.-X., Banfield, J. F., St John, E., Reysenbach, A.-L., Stott, M. B., Schramm, A., Kjeldsen, K. U., Teske, A. P., Baker, B. J., and Ettema T. J. G.: Inference and reconstruction of the heimdallarchaeial ancestry of eukaryotes, Nature, 618, 992–999, https://doi.org/10.1038/s41586-023-06186-2, 2023.

Findlay, A. J.: Microbial impact on polysulfide dynamics in the environment, FEMS Microbiol. Lett., 363, fnw103, https://doi.org/10.1093/femsle/fnw103, 2016.

Findlay, A. J., Gartman, A., MacDonald, D. J., Hanson, T. E., Shaw, T. J., and Luther III, G. W.: Distribution and size fractionation of elemental sulfur in aqueous environments: The Chesapeake Bay and Mid-Atlantic Ridge, Geochim. Cosmochim. Ac., 142, 334–348, https://doi.org/10.1016/j.gca.2014.07.032, 2014.

Fouquet, Y. and Pelleter, E.: HERMINE cruise, RV Pourquoi pas?, French Oceanographic Cruises, https://doi.org/10.17600/17000200, 2017.

Fouquet, Y., Henry, K., Knott, R., and Cambon, P.: Geochemical section of the TAG hydrothermal mound, Oceanographic Literature Review, 45, 1356, ISSN 0967-0653, 1996.

Fulignati P., Clay Minerals in Hydrothermal Systems, Minerals 10, 919, https://doi.org/10.3390/min10100919, 2020.

Gartman, A., Findlay, A. J., and Luther III, G. W.: Nanoparticulate pyrite and other nanoparticles are a widespread component of

hydrothermal vent black smoker emissions, Chem. Geol., 366, 32–41, https://doi.org/10.1016/j.chemgeo.2013.12.013, 2014.

German, C. R. and Von Damm, K.: Hydrothermal processes, edited by: Holland, H. D. and Turekian, K. K., Treatise on Geochemistry, Elsevier, Oxford, 191–233, ISBN 0080437516, 9780080437514, 2006.

Gorlas, A., Marguet, E., Gill, S., Geslin, C., Guigner, J. M., Guyot, F., and Forterre, P.: Sulfur vesicles from Thermococcales: A possible role in sulfur detoxifying mechanisms, Biochimie, 118, 356–364, https://doi.org/10.1016/j.biochi.2015.07.026, 2015.

Gorlas, A., Jacquemot, P., Guigner, J. M., Gill, S., Forterre, P., and Guyot, F.: Greigite nanocrystals produced by hyperthermophilic archaea of Thermococcales order, PLoS One, 13, e0201549, https://doi.org/10.1371/journal.pone.0201549, 2018.

Gorlas, A., Mariotte, T., Morey, L., Truong, C., Bernard, S., Guigner, J.-M., Oberto, J., Baudin, F., Landrot, G., Baya, C., Le Pape, P., Morin, G., Forterre, P., and Guyot, F.: Precipitation of greigite and pyrite induced by Thermococcales: an advantage to live in Fe- and S-rich environments?, Environ. Microbiol., 24, 626–642, https://doi.org/10.1111/1462-2920.15915, 2022.

Grant, H. L., Hannington, M. D., Petersen, S., Frische, M., and Fuchs, S. H.: Constraints on the behavior of trace elements in the actively-forming TAG deposit, Mid-Atlantic Ridge, based on LA-ICP-MS analyses of pyrite, Chem. Geol., 498, 45–71, https://doi.org/10.1016/j.chemgeo.2018.08.019, 2018.

Hannington, M., Jamieson, J., Monecke, T., Petersen, S., and Beaulieu, S.: The abundance of seafloor massive sulfide deposits, Geology, 39, 1155–1158, https://doi.org/10.1130/G32468.1, 2011.

Haymon, R. M.: Growth history of hydrothermal black smoker chimneys, Nature, 301, 695–698, https://doi.org/10.1038/301695a0, 1983.

Haymon, R. M. and Kastner, M.: The formation of high temperature clay minerals from basalt alteration during hydrothermal discharge on the East Pacific Rise axis at 21 N, Geochim. Cosmochim. Ac., 50, 1933–1939, https://doi.org/10.1016/0016-7037(86)90249-8, 1986.

Heinen, W. and Lauwers, A. M.: Organic sulfur compounds resulting from the interaction of iron sulfide, hydrogen sulfide and carbon dioxide in an anaerobic aqueous environment, Origins Life Evol. B., 26, 131–150, https://doi.org/10.1007/BF01809852, 1996.

Hekinian, R., Fevrier, M., Bischoff, J. L., Picot, P., and Shanks, W. C.: Sulfide deposits from the East Pacific Rise near 21 N, Science, 207, 1433–1444, https://doi.org/10.1126/science.207.4438.1433, 1980.

Holden, J. F. and Adams, M. W.: Microbe–metal interactions in marine hydrothermal environments, Curr. Opin. Chem. Biol., 7, 160–165, https://doi.org/10.1016/S1367-5931(03)00026-7, 2003.

Houghton, J. L. and Seyfried Jr., W. E.: An experimental and theoretical approach to determining linkages between geochemical variability and microbial biodiversity in seafloor hydrothermal chimneys, Geobiology, 8, 457–470, https://doi.org/10.1111/j.1472-4669.2010.00255.x, 2010.

Hu, S. Y., Barnes, S. J., Glenn, A. M., Pagès, A., Parr, J., MacRae, C., and Binns, R.: Growth history of sphalerite in a modern sea floor hydrothermal chimney revealed by electron backscattered diffraction, Econ. Geol., 114, 165–176, https://doi.org/10.5382/econgeo.2019.4626, 2019.

Hu, S. Y., Barnes, S. J., Pagès, A., Parr, J., Binns, R., Verrall, M., Quadir, Z., Rickard, W., Liu, W., Fougerouse, D., Grice, K., Schonevald, L., Ryan, C., and Paterson, D.: Life on the edge: microbial biomineralization in an arsenic-and lead-rich deep-sea hydrothermal vent, Chem. Geol., 533, 119438, https://doi.org/10.1016/j.chemgeo.2019.119438, 2020.

Huber, C. and Wachtershauser, G.: Activated acetic acid by carbon fixation on (Fe, Ni) S under primordial conditions, Science, 276, 245–247, https://doi.org/10.1126/science.276.5310.245, 1997.

Humphris, S. E. and Kleinrock, M. C.: Detailed morphology of the TAG active hydrothermal mound: Insights into its formation and growth, Geophys. Res. Lett., 23, 3443–3446, https://doi.org/10.1029/96GL03079, 1996.

Jannasch, H. W.: Microbial interactions with hydrothermal fluids, Geoph. Monog. Series, 91, 273–296, https://doi.org/10.1029/GM091p0273, 1995.

Juniper, S. K., Bird, D. F., Summit, M., Vong, M. P., and Baker, E. T.: Bacterial and viral abundances in hydrothermal event plumes over northern Gorda Ridge, Deep-Sea Res. Pt. II, 45, 2739–2749, https://doi.org/10.1016/S0967-0645(98)00091-5, 1998.

Konn, C., Donval, J. P., Guyader, V., Germain, Y., Alix, A. S., Roussel, E., and Rouxel, O.: Extending the dataset of fluid geochemistry of the Menez Gwen, Lucky Strike, Rainbow, TAG and Snake Pit hydrothermal vent fields: Investigation of temporal stability and organic contribution, Deep-Sea Res. Pt. I, 179, 103630, https://doi.org/10.1016/j.dsr.2021.103630, 2022.

Kvenvolden, K. A. and Simoneit, B. R.: Hydrothermally derived petroleum: Examples from Guaymas Basin, Gulf of California, and Escanaba Trough, Northeast Pacific Ocean, AAPG Bull., 74, 223–237, 1990.

Lafitte, M., Maury, R., and Perseil, E. A. : Analyse mineralogique de cheminees a sulfures de la dorsale Est Pacifique (13 N), Miner. Deposita, 19, 274–282, https://doi.org/10.1007/BF00204380, 1984.

Lalou, C., Thompson, G., Rona, P. A., Brichet, E., and Jehanno, C.: Chronology of selected hydrothermal Mn oxide deposits from the transatlantic geotraverse "TAG" area, Mid-Atlantic Ridge 26° N, Geochim. Cosmochim. Ac., 50, 1737–1743, 1986.

Lalou, C., Reyss, J. L., Brichet, E., Arnold, M., Thompson, G., Fouquet, Y., and Rona, P. A.: New age data for Mid-Atlantic Ridge hydrothermal sites: TAG and Snakepit chronology revisited, J. Geophys. Res.-Sol. Ea., 98, 9705–9713, https://doi.org/10.1029/92JB01898, 1993.

Lalou, C., Reyss, J. L., Brichet, E., Rona, P. A., and Thompson, G.: Hydrothermal activity on a 10^5-year scale at a slow-spreading ridge, TAG hydrothermal field, Mid-Atlantic Ridge 26° N, J. Geophys. Res.-Sol. Ea., 100, 17855–17862, https://doi.org/10.1029/95JB01858, 1995.

Langmuir, C., Humphris, S., Fornari, D., VanDover, C., VonDamm, K., Tivey, M., Colodner, D., Charlou, J.-L., Desonie, D., Wilson, C., Fouquet, Y., Klinkhammer, G., and Bougault, H.: Hydrothermal vents near a mantle hot spot: the Lucky Strike vent field at 37 degrees N on the Mid-Atlantic Ridge, Earth Planet Sc. Lett., 148, 69–91, https://doi.org/10.1016/S0012-821X(97)00027-7, 1997.

Le Guillou, C., Bernard, S., De la Pena, F., and Le Brech, Y.: XANES-based quantification of carbon functional

group concentrations, Anal. Chem., 90, 8379–8386, https://doi.org/10.1021/acs.analchem.8b00689, 2018.

Li, J., Benzerara, K., Bernard, S., and Beyssac, O.: The link between biomineralization and fossilization of bacteria: insights from field and experimental studies, Chem. Geol., 359, 49–69, https://doi.org/10.1016/j.chemgeo.2013.09.013, 2013.

Li, J., Bernard, S., Benzerara, K., Beyssac, O., Allard, T., Cosmidis, J., and Moussou, J.: Impact of biomineralization on the preservation of microorganisms during fossilization: An experimental perspective, Earth Planet. Sc. Lett., 400, 113–122, https://doi.org/10.1016/j.epsl.2014.05.031, 2014.

Lin, T., Ver Eecke, H., Breves, E., Dyar, M., Jamieson, J., Hannington, M., Dahle, H., Bishop, J., Lane, M., Butterfield, D., Kelley, D., Lilley, M., Baross, J., and Holden, J.: Linkages between mineralogy, fluid chemistry, and microbial communities within hydrothermal chimneys from the Endeavour segment, Juan de Fuca ridge, Geochem. Geophy. Geosy., 17, 300–323, https://doi.org/10.1002/2015GC006091, 2016.

Luther III, G. W., Church, T. M., Scudlark, J. R., and Cosman, M.: Inorganic and organic sulfur cycling in salt-marsh pore waters, Science, 232, 746–749, https://doi.org/10.1126/science.232.4751.746, 1986.

MacLeod, F., Kindler, G. S., Wong, H. L., Chen, R., and Burns, B. P.: Asgard archaea: diversity, function, and evolutionary implications in a range of microbiomes, AIMS Microbiology, 48, 48–61, https://doi.org/10.3934/microbiol.2019.1.48, 2019.

Mansor, M.: Isotopic and Trace Metal Geochemistry of Calcite, Gypsum, and Pyrite as Proxies for Ancient Life and Environments, The Pennsylvania State University ProQuest Dissertations & Theses, 10629089, 2017.

Mansor, M., Berti, D., Hochella Jr, M. F., Murayama, M., and Xu, J.: Phase, morphology, elemental composition, and formation mechanisms of biogenic and abiogenic Fe-Cu-sulfide nanoparticles: A comparative study on their occurrences under anoxic conditions, Am. Mineral., 104, 703–717, https://doi.org/10.2138/am-2019-6848, 2019.

Marin-Carbonne, J., Remusat, L., Sforna, M. C., Thomazo, C., Cartigny, P., and Philippot, P.: Sulfur isotope's signal of nanopyrites enclosed in 2.7 Ga stromatolitic organic remains reveal microbial sulfate reduction, Geobiology, 16, 121–138, https://doi.org/10.1111/gbi.12275, 2018.

Marin-Carbonne, J., Busigny, V., Miot, J., Rollion-Bard, C., Muller, E., Drabon, N., and Philippot, P.: In Situ Fe and S isotope analyses in pyrite from the 3.2 Ga Mendon Formation (Barberton Greenstone Belt, South Africa): Evidence for early microbial iron reduction, Geobiology, 18, 306–325, https://doi.org/10.1111/gbi.12385, 2020.

Marin-Carbonne, J., Decraene, M. N., Havas, R., Remusat, L., Pasquier, V., Alléon, J., and Thomazo, C.: Early precipitated micropyrite in microbialites: a time capsule of microbial sulfur cycling, Geochem. Perspect. Lett. 21, 7–12, https://doi.org/10.7185/geochemlet.2209, 2022.

McCollom, T. M. and Seewald, J. S.: Abiotic synthesis of organic compounds in deep-sea hydrothermal environments, Chemi. Rev., 107, 382–401, https://doi.org/10.1021/cr0503660, 2007.

McCollom, T. M., Lollar, B. S., Lacrampe-Couloume, G., and Seewald, J. S.: The influence of carbon source on abiotic organic synthesis and carbon isotope fractionation under hydrothermal conditions, Geochim. Cosmochim. Ac., 74, 2717–2740, https://doi.org/10.1016/j.gca.2010.02.008, 2010.

Meier, D., Pjevac, P., Bach, W., Markert, S., Schweder, T., Jamieson, J., Petersen, S., Amann, R., and Meyerdierks, A: Microbial metal-sulfide oxidation in inactive hydrothermal vent chimneys suggested by metagenomic and metaproteomic analyses, Environmen. Microbiol., 21, 682–701, https://doi.org/10.1111/1462-2920.14514, 2019.

Murowchick, J. B. and Barnes, H. L.: Effects of temperature and degree of supersaturation on pyrite morphology, Am. Mineral., 72, 1241–1250, ISSN 1945-3027, 1987.

Nabeh, N., Brokaw, C., and Picard, A.: Quantification of organic carbon sequestered by biogenic iron sulfide minerals in long-term anoxic laboratory incubations, Front. Microbiol., 13, 662219, https://doi.org/10.3389/fmicb.2022.662219, 2022.

Nielsen, M. H., Li, D., Zhang, H., Aloni, S., Han, Y-J., Frandsen, C., Seto, J., Banfield, J. F., Cölfen, H., and De Yoreo, J. J.: Investigating processes of nanocrystal formation and transformation via liquid cell TEM, Microsc. Microanal. 20, 425–436, https://doi.org/10.1017/S1431927614000294, 2014.

Pelleter, E. and Cathalot, C.: HERMINE2 cruise, RV Pourquoi pas?, French Oceanographic Cruises, https://doi.org/10.17600/18001851, 2022.

Pontbriand, C. W. and Sohn, R. A.: Microearthquake evidence for reaction-driven cracking within the Trans-Atlantic Geotraverse active hydrothermal deposit, J. Geophys. Res.-Sol. Ea., 119, 822–839, https://doi.org/10.1002/2013JB010110, 2014.

Rodrigues-Oliveira, T., Wollweber, F., Ponce-Toledo, R. I., Xu, J., Rittmann, S. K. R., Klingl, A., Pilhofer, M., and Schleper, C.: Actin cytoskeleton and complex cell architecture in an Asgard archaeon, Nature, 613, 332–339, https://doi.org/10.1038/s41586-022-05550-y, 2023.

Rona, P. A.: TAG hydrothermal field: Mid-Atlantic Ridge crest at latitude 26 N, J. Geol. Soc. London, 137, 385–402, 1980.

Rona, P. A., Thompson, G., Mottl, M. J., Karson, J. A., Jenkins, W. J., Graham, D., Mallette, M., Von Damm, K., and Edmond, J. M.: Hydrothermal Activity at the Trans-Atlantic Geotraverse Hydrothermal Field, Mid-Atlantic Ridge Crest at 26° N, J. Geophys. Res., 89, 11365–11377, https://doi.org/10.1029/JB089iB13p11365, 1984.

Rona, P. A., Klinkhammer, G., Nelsen, T. A., Trefry, J. H., and Elderfield, H.: Black smokers, massive sulphides and vent biota at the Mid-Atlantic Ridge, Nature, 321, 33–37, https://doi.org/10.1038/321033a0, 1986.

Rona, P. A., Hannington, M. D., Raman, C. V., Thompson, G., Tivey, M. K., Humphris, S. E., Lalou, C., and Petersen, S.: Active and relict seafloor hydrothermal mineralization at the TAG hydrothermal field Mid-Atlantic Ridge, Econ. Geol., 18, 1989–2017, https://doi.org/10.2113/gsecongeo.88.8.1989, 1993.

Runge, E. A., Mansor, M., Kappler, A., and Duda, J.-P.: Microbial biosignatures in ancient deep-sea hydrothermal sulfides, Geobiology, 21, 355–377, https://doi.org/10.1111/gbi.12539, 2022.

Russell, M. J., Daniel, R. M., Hall, A. J., and Sherringham, J. A.: A hydrothermally precipitated catalytic iron sulphide membrane as a first step toward life, J. Mol. Evol., 39, 231–243, https://doi.org/10.1007/BF00160147, 1994.

Schiffbauer, J. and Xiao, S.: Novel application of focused ion beam electron microscopy (FIB-EM) in preparation and analysis of microfossil ultrastructures: A new view of complex-

ity in early Eukaryotic organisms, PALAIOS, 24, 616–626, https://doi.org/10.2110/palo.2009.p09-003r, 2009.

Schrenk, M., Kelley, D., Delaney, J., and Baross, J.: Incidence and diversity of microorganisms within the walls of an active deep-sea sulfide chimney, Appl. Environ. Microb., 69, 3580–3592, https://doi.org/10.1128/AEM.69.6.3580-3592.2003, 2003.

Schwarzenbach, G. and Fischer, A.: Die acidität der Sulfane und die Zusammensetzung wässeriger Polysulfidlösungen, Helv. Chim. Acta, 169, 1365–1390, https://doi.org/10.1002/hlca.19600430521, 1960.

Scott, R. B., Rona, P. A., Mc Gregor, B. A., and Scott, M. R.: The TAG Hydrothermal Field, Nature, 251, 301–302, https://doi.org/10.1038/251301a0, 1974.

Sheik, C. S., Anantharaman, K., Breier, J. A., Sylvan, J. B., Edwards, K. J., and Dick, G. J.: Spatially resolved sampling reveals dynamic microbial communities in rising hydrothermal plumes across a back-arc basin, ISME J., 9, 1434–1445, https://doi.org/10.1038/ismej.2014.228, 2015.

Simoneit, B. R. T.: Aqueous high-temperature and high-pressure organic geochemistry of hydrothermal vent systems, Geochim. Cosmochim. Ac. 57, 3231–3243, https://doi.org/10.1016/0016-7037(93)90536-6, 1993.

Spang, A., Saw, J. H., Jørgensen, S. L., Zaremba-Niedzwiedzka, K., Martijn, J., Lind, A. E., van Eijk, R., Schleper, C., Guy, L., and Ettema, T. J. G.: Complex archaea that bridge the gap between prokaryotes and eukaryotes, Nature, 521, 173–179, https://doi.org/10.1038/nature14447, 2015.

Šrot, V. Š., Rečnik, A., Scheu, C., Šturm, S., and Mirtič, B.: Stacking faults and twin boundaries in sphalerite crystals from the Trepca mines in Kosovo, Am. Mineral., 88, 1809–1816, https://doi.org/10.2138/am-2003-11-1222, 2003.

Stein, C. and Stein, S.: Constraints on hydrothermal Heat-Flux through the oceanic lithosphere from global heat-flow, J. Geophys. Res., 99, 3081–3095, https://doi.org/10.1029/93JB02222, 1994.

Steudel, R.: Mechanism for the formation of elemental sulfur from aqueous sulfide in chemical and microbiological desulfurization processes, Ind. Eng. Chem. Res., 35, 1417–1423, https://doi.org/10.1021/ie950558t, 1996.

Swaraj, S., Stanescu, S., Rioult, M., Besson, A., and Hitchcock, A. P.: Performance of the HERMES beamline at the carbon K-edge, J. Phys. Conf. Ser., 849, 012046, https://doi.org/10.1088/1742-6596/849/1/012046, 2017.

Takai, K., Nakamura, K., Toki, T., Tsunogai, U., Miyazaki, M., Miyazaki, J., Hirayama, H., Nakagawa, S., Nunoura, T., and Horikoshi, K.: Cell proliferation at 122°C and isotopically heavy CH_4 production by a hyperthermophilic methanogen under high-pressure cultivation, P. Natl. Acad. Sci. USA, 105, 10949–10954, https://doi.org/10.1073/pnas.0712334105, 2008.

Templeton, A., Knowles, E., Eldridge, D., Arey, B., Dohnalkova, A., Webb, S., Bailey, B., Tebo, B., and Staudigel, H.: A seafloor microbial biome hosted within incipient ferromanganese crusts, Nat. Geosci., 2, 872–876, https://doi.org/10.1038/ngeo696, 2009.

Tivey, M.: The influence of hydrothermal fluid composition and advection rates on black smoker chimney mineralogy: insights from modelling transport and reaction, Geochim. Cosmochim. Ac., 59, 1933–1949, https://doi.org/10.1016/0016-7037(95)00118-2, 1995.

Tivey, M. K. and Delaney, J. R.: Growth of large sulfide structures on the endeavour segment of the Juan de Fuca Ridge, Earth Planet. Sc. Lett., 77, 303–317, https://doi.org/10.1016/0012-821X(86)90142-1, 1986.

Tivey, M. A., Bradley, A. M., Joyce T. M., and Kadko D: Insights into tide-related variability at seafloor hydrothermal vents from time-series temperature measurements, Earth Planet. Sc. Lett., 202, 693–707, https://doi.org/10.1016/S0012-821X(02)00801-4, 2002.

Tivey, M. A., Schouten, H., and Kleinrock, M. C.: A near-bottom magnetic survey of the Mid-Atlantic Ridge axis at 26° N: Implications for the tectonic evolution of the TAG segment, J. Geophys. Res.-Sol. Ea., 108, 1–13, https://doi.org/10.1029/2002JB001967, 2003.

Thompson, G., Mottl, M. J., and Rona, P. A.: Morphology, Mineralogy and Chemistry of Hydrothermal Deposits from the TAG Area, 26° N Mid-Atlantic Ridge, Chem. Geol., 49, 243–257, https://doi.org/10.1016/0009-2541(85)90159-7, 1985.

Thompson, G., Humphris, S. E., Schroeder, B., and Sulanowska, M.: Active Vents and Massive Sulfides at 26° N (TAG) and 23° N (Snake Pit) on the Mid-Atlantic Ridge, Can. Mineral., 26, 697–711, 1988.

Truong, C., Bernard, S., Le Pape, P., Morin, G., Baya, C., Merrot, P., Gorlas, A., and Guoyt, F.: Production of carbon-containing pyrite spherules induced by hyperthermophilic Thermococcales: a biosignature?, Front. Microbiol., 14, 1–15, https://doi.org/10.3389/fmicb.2023.1145781, 2023.

Vladimirov, M. G., Ryzhkov, Y. F., Alekseev, V. A., Bogdanovskaya, V. A., Otroshchenko, V. A., and Kritsky, M. S.: Electrochemical Reduction of Carbon Dioxide on Pyrite as a Pathway for Abiogenic Formation of Organic Molecules, Origins Life Evol. B., 34, 347–360, https://doi.org/10.1023/B:ORIG.0000029883.18365.af, 2004.

Von Damm, K. L.: Hydrothermal vent fluids, chemistry of. Elements of Physical Oceanography: A derivative of the Encyclopedia of Ocean Sciences, edited by: Steele, J. H., Thorpe, S. A., and Turekian, K. K., 81–88, ISBN-10 0080964850, 2001.

Wächtershäuser, G.: Evolution of the first metabolic cycles, P. Nat. Acad. Sci. USA, 87, 200–204, https://doi.org/10.1073/pnas.87.1.200, 1990.

Wang, J., Morin, C., Li, L., Hitchcock, A. P., Scholl, A., and Doran, A.: Radiation damage in soft X-ray microscopy, J. Electron Spectrosc., 170, 25–36, https://doi.org/10.1016/j.elspec.2008.01.002, 2009.

Wang, S., Li, C., Li, B., Dang, Y., Ye, J., Zhu, Z., Zhang, L., and Shi, X.: Constraints on fluid evolution and growth processes of black smoker chimneys by pyrite geochemistry: A case study of the Tongguan hydrothermal field, South Mid-Atlantic Ridge, Ore Geol. Rev., 140, 104410, https://doi.org/10.1016/j.oregeorev.2021.104410, 2022.

Weiss, M. C., Sousa, F. L., Mrnjavac, N., Neukirchen, S., Roettger, M., Nelson-Sathi, S., and Martin, W. F.: The physiology and habitat of the last universal common ancestor, Nat. Microbiol., 1, 16116, https://doi.org/10.1038/nmicrobiol.2016.116, 2016.

Wheat, C., Jannasch, W., Plant, J., Moyer, C, Sansone, F., and McMurtry, G.: Continuous sampling of hydrothermal fluids from Loihi Sea mount after the 1996 event, J. Geophys. Res., 105, 19353–19367, https://doi.org/10.1029/2000JB900088, 2000.

White, S. N., Humphris, S. E., and Kleinrock, M. C.: New observations on the distribution of past and present hydrothermal activity in the TAG area of the Mid-Atlantic Ridge (26° 08'N), Mar. Geophys. Res., 20, 41–56, https://doi.org/10.1023/A:1004376229719, 1998.

Winn, C., Karl, D., and Massoth, G.: Microorganisms in deep-sea hydrothermal plumes, Nature, 320, 744–746, https://doi.org/10.1038/320744a0, 1986.

Wirth, R.: Colonization of black smokers by hyperthermophilic microorganisms, Trends Microbiol., 25, 92–99, https://doi.org/10.1016/j.tim.2016.11.002, 2017.

Wirth, R., Luckner, M., and Wanner, G.: Validation of a hypothesis: colonization of black smokers by hyperthermophilic microorganisms, Front. Microbiol., 9, 524, https://doi.org/10.3389/fmicb.2018.00524, 2018.

Xu, J., Murayama, M., Roco, C. M., Veeramani, H., Michel, F. M., Rimstidt, J. D., Winkler, C., and Hochella, Jr. M. F.: Highly-defective nanocrystals of ZnS formed via dissimilatory bacterial sulfate reduction: A comparative study with their abiogenic analogues, Geochim. Cosmochim. Ac., 180, 1–14, https://doi.org/10.1016/j.gca.2016.02.007, 2016.

Yücel, M., Gartman, A., Chan, C. S., and Luther, G. W.: Hydrothermal vents as a kinetically stable source of iron-sulphide-bearing nanoparticles to the ocean, Nat. Geosci., 4, 367–371, https://doi.org/10.1038/ngeo1148, 2011.

Yücel, M., Sevgen, S., and Le Bris, N.: Soluble, colloidal, and particulate iron across the hydrothermal vent mixing zones in broken spur and rainbow, mid-atlantic ridge, Front. Microbiol., 12, 631885, https://doi.org/10.3389/fmicb.2021.631885, 2021.

Zhu, W., Tivey, M. K., Gittings, H., and Craddock, P. R.: Permeability-porosity relationships in seafloor vent deposits: Dependence on pore evolution processes. J. Geophys. Res.-Solid Ea., 112, 1–15, https://doi.org/10.1029/2006JB004716, 2007.